






RESEARCH ARTICLE | JULY 31 2023

# Achieving superhydrophobicity of the FeCoCrMnNi surface via synergistic laser texturing and low temperature annealing

Chao Wang ; Hu Huang  ; Mingming Cui; Zhiyu Zhang ; Lin Zhang; Jiwang Yan 

 Check for updates

*J. Laser Appl.* 35, 032013 (2023)

<https://doi.org/10.2351/7.0001053>



CrossMark



Journal of  
Laser Applications

[Learn More](#)



RAPID TIME  
TO ACCEPTANCE



COMMUNITY  
DRIVEN



EXPANSIVE  
COVERAGE



PRESTIGIOUS  
EDITORIAL BOARD



EXTENSIVE  
MARKETING

# Achieving superhydrophobicity of the FeCoCrMnNi surface via synergistic laser texturing and low temperature annealing

Cite as: J. Laser Appl. **35**, 032013 (2023); doi: [10.2351/7.0001053](https://doi.org/10.2351/7.0001053)

Submitted: 13 May 2023 · Accepted: 18 July 2023 ·

Published Online: 31 July 2023



Chao Wang,<sup>1</sup>  Hu Huang,<sup>1,a)</sup>  Mingming Cui,<sup>1</sup> Zhiyu Zhang,<sup>2</sup>  Lin Zhang,<sup>3</sup> and Jiwang Yan<sup>3</sup> 

## AFFILIATIONS

<sup>1</sup>Key Laboratory of CNC Equipment Reliability, Ministry of Education, School of Mechanical and Aerospace Engineering, Jilin University, Changchun, Jilin 130022, China

<sup>2</sup>Key Laboratory of Optical System Advanced Manufacturing Technology, Changchun Institute of Optics, Fine Mechanics and Physics, Chinese Academy of Sciences, Changchun 130033, China

<sup>3</sup>Department of Mechanical Engineering, Faculty of Science and Technology, Keio University, Yokohama 223-8522, Japan

<sup>a)</sup>Author to whom correspondence should be addressed; electronic mail: [huanghu@jlu.edu.cn](mailto:huanghu@jlu.edu.cn)

## ABSTRACT

Superhydrophobic surfaces are highly desirable due to their remarkable water-repellent behavior. Laser texturing with subsequent low surface energy modification is a versatile strategy for creating such surfaces. In this study, via synergistic laser texturing and low temperature annealing, superhydrophobicity was first attempted to be achieved on the FeCoCrMnNi surface. By optimizing the laser parameters, the arrays with large depth-to-width ratios were constructed. Subsequently, by annealing at a low temperature, the transition process from superhydrophilicity to superhydrophobicity was successfully achieved on the FeCoCrMnNi surface. The effects of the hatching interval on the wettability were investigated, and the mechanism of wettability transition for FeCoCrMnNi was discussed. According to the experimental results and analysis, the textured surfaces exhibited excellent superhydrophobicity at different hatching intervals and a maximum contact angle of 165° was obtained. Furthermore, the created superhydrophobic surfaces possessed good liquid capture and self-cleaning capabilities and enabled magnification for optical imaging. The wettability transition after low temperature annealing was attributed to the absorption of airborne organic compounds. This study provides an efficient, clean, and versatile strategy to achieve superhydrophobicity of the FeCoCrMnNi surface by laser processing.

Key words: high-entropy alloys, laser texturing, superhydrophobicity, depth-to-width ratio

Published under an exclusive license by Laser Institute of America. <https://doi.org/10.2351/7.0001053>

## I. INTRODUCTION

Being different from conventional alloy design concepts, high-entropy alloys (HEAs) consist of at least five principal elements in nearly equal atomic ratios.<sup>1</sup> Currently, FeCoCrMnNi (also known as the Cantor alloy), composed of fcc single-phase solid solution, has gained significant attention.<sup>2</sup> Due to mechanical nanotwinning-induced strain hardening during deformation, FeCoCrMnNi exhibits remarkable mechanical properties, including high fracture toughness (over 200 MPa m<sup>1/2</sup>) and tensile strength (up to 1 GPa) at a cryogenic temperature of 77 K in liquid nitrogen.<sup>3–5</sup> In addition, it displays excellent corrosion resistance,<sup>6</sup> structural stability,<sup>7</sup> and swelling

tolerance (more than 40 times that of nickel),<sup>8</sup> owing to its severe lattice distortion and sluggish diffusion effects. These properties make FeCoCrMnNi a preferred candidate for components in some harsh service environments.<sup>9</sup> However, as a typical metallic alloy, its inherent hydrophilic nature renders it susceptible to wetting by various liquids. Direct contact with liquids at the solid-liquid interface increases its failure risk in humid, cryogenic, and other service conditions. Superhydrophobic surfaces have been employed in various applications such as self-cleaning,<sup>10</sup> anti-icing,<sup>11</sup> anticorrosion,<sup>12</sup> and heat transfer.<sup>13</sup> Therefore, achieving superhydrophobicity of the FeCoCrMnNi surface could prolong its service life and expand its potential applications.

06 March 2024 02:15:03

Constructing rough surfaces with subsequent low surface energy modification represents a highly versatile strategy for creating a superhydrophobic surface.<sup>14</sup> This approach has been developed into various methods. For example, by spraying, a coating composed of fluorinated polymers mixed with nanoparticles was prepared to achieve a superhydrophobic glass surface.<sup>15</sup> Via photolithography, an inverted pyramidal array was fabricated on the silicon surface, and then assisted by fluorinated polymers, a superhydrophobic surface with high mechanical stability was obtained.<sup>16</sup> Using ion beam etching and chemical vapor deposition, hierarchical structures with conformal fluoropolymer layers were constructed on the copper surface to achieve superhydrophobicity.<sup>12</sup> For the fabrication of superhydrophobic surface microstructures on metallic materials, laser processing has received considerable attention due to its low cost, controllable patterns, and precision machining.<sup>17,18</sup> However, rare studies have been reported on the preparation of the superhydrophobic surface microstructures on FeCoCrMnNi via laser processing.

Fresh laser textured metal surfaces generally exhibit high hydrophilicity, which can be transformed into superhydrophobicity by reducing surface free energy. Traditionally, fluorinated/silanized organics with low surface energy have been used for surface modification to create superhydrophobic surfaces.<sup>19,20</sup> However, this method is costly and environmental-unfriendly. Some studies<sup>21,22</sup> have shown that samples can spontaneously transition from hydrophilicity to superhydrophobicity when they are exposed to ambient air, without any chemical treatment; furthermore, annealing at the low temperature could accelerate this transition.<sup>23,24</sup> This process has successfully produced superhydrophobic surfaces on various alloys such as stainless steel,<sup>24</sup> copper,<sup>25</sup> aluminum,<sup>22</sup> and titanium alloys.<sup>26</sup> However, the underlying mechanism of this transition process is a subject of debate for different metals. On the stainless steel surface, this transition was attributed to the decomposition of carbon dioxide into carbon through active magnetite.<sup>23,27</sup> On the copper surface, some studies suggested that this transition was related to the deoxygenation of CuO to form Cu<sub>2</sub>O.<sup>28,29</sup> For aluminum alloys, recent studies had ascribed this transition to the absorption of airborne organic compounds.<sup>21,22</sup> Nevertheless, most studies have focused on conventional alloys dominated by a single element, and it is unclear whether this transition will also occur on HEAs with multiple elements and what the underlying mechanisms might be.

In this study, regular arrays with large depth-to-width ratios were successfully constructed on the FeCoCrMnNi surface via nanosecond laser texturing. By subjecting the textured surfaces to the low-temperature annealing treatment, superhydrophobic surfaces were created within a few hours. The effects of hatching intervals on wettability were also investigated. Furthermore, the mechanism of wettability transition for FeCoCrMnNi was elucidated by analyzing the changes in surface chemical compositions. This finding demonstrates the potential applications of superhydrophobic surfaces through droplet bouncing, self-cleaning, and optical images of droplets.

## II. EXPERIMENTS

The equiatomic FeCoCrMnNi HEA specimens were prepared by vacuum arc melting. The cast ingot was cut into samples with

TABLE I. Experimental parameters.

Sample material	FeCoCrMnNi
Laser power, $P$ (W)	4.2, 6.0, 7.8, 9.7, 11.6, 13.4
Laser scanning speed, $v$ (mm/s)	10
Number of scans, $N$	1, 3, 5, 7
Hatching interval, $d$ (mm)	50, 100, 150, 200
Atmosphere	Air

dimensions of  $25 \times 25 \times 3$  mm<sup>3</sup> using electrical discharge machining wire-cutting. The samples were sequentially ground using 200#, 400#, 800#, 1200#, and 2000# sandpapers and polished to a mirror-like finish. Then, the samples were degreased with acetone by ultrasonic cleaning.

The prepared samples were textured by using a nanosecond pulse laser (SP-050P-A-EP-Z-F-Y, SPI, UK) with a wavelength of 1064 nm and a pulse width of 7 ns. The laser energy has a Gaussian distribution ( $M^2 < 2$ ), and it is focused on the plane with a diameter of  $43 \mu\text{m}$ . To construct arrays with large depth-to-width ratios, single-line scanning experiments were performed with various laser powers and number of scans. The laser scanning speed was kept at 10 mm/s. To ensure the accuracy and reliability of the results, three scans were conducted for each condition. Additionally, five areas along each scan line were selected for measurement. The optimal laser parameters were selected based on the results obtained from the experiments, and the detailed experimental parameters were listed in Table I. After the laser texturing, the samples were subjected to a low-temperature annealing treatment at 150 °C for 4 h, and the fabrication process was illustrated in Fig. 1. The textured surfaces were observed by the laser scanning confocal microscope (OLS5100, Olympus, Japan) and scanning electron microscope (SEM, JSM-IT500A, JEOL, Japan). The contact angles of textured surfaces were measured using a contact angle measuring meter (OAS60, NBSI, China) with  $5 \mu\text{l}$  de-ionized water. The textured surfaces were characterized by x-ray diffraction (XRD, D8Discover, Bruker, Germany) and x-ray electron spectroscopy (XPS, JPS-9010TR, JEOL, Japan). The dynamics of droplet impact were captured by a high-speed camera (Phantom VEO 410L-18G) at the frame rate of 10 000 fps, and the deformation of drops during impingement was analyzed by Phantom Video Player software.

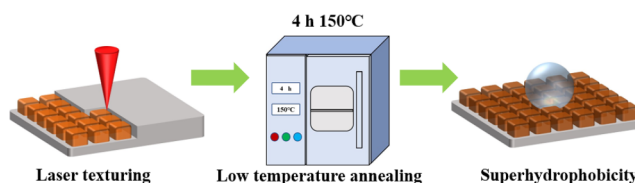


FIG. 1. The fabrication process of the superhydrophobic FeCoCrMnNi surface.

III. RESULTS AND DISCUSSION

As shown in Fig. 2(a), the contact angle of an ideal plane can be expressed by classical Young’s model,<sup>30</sup> and that is

$$\cos \theta_Y = \frac{\gamma_{SG} - \gamma_{SL}}{\gamma_{LG}}, \tag{1}$$

where  $\gamma_{SG}$ ,  $\gamma_{SL}$ ,  $\gamma_{LG}$  represent the surface tension for interfaces between solid S, liquid L, gas G, respectively. As shown in Fig. 2(b), the contact angle of rough surfaces can be described by the Cassie–Baxter model,<sup>31</sup> and that is

$$\cos \theta_{CB} = f_1 \cos \theta_1 + f_2 \cos \theta_2, \tag{2}$$

where  $\theta_1$  and  $\theta_2$  are the contact angle for liquid on the ideal solid and gas surfaces;  $f_1$  and  $f_2$  are the area fractions of solid-liquid and gas-liquid, respectively. Since  $f_1 + f_2 = 1$  and  $\theta_2 = 180^\circ$ , the contact

angle can be further written as

$$\cos \theta_{CB} = f_1 (\cos \theta_1 + 1) - 1. \tag{3}$$

According to Eq. (3), a large contact angle can be achieved by decreasing the area fractions  $f_1$  of solid-liquid. To achieve superhydrophobicity on the FeCoCrMnNi surface, surface microstructures with large depth-to-width ratios are constructed, which can store more gas at the solid-liquid interface and reduce the contact area of solid-liquid, thereby promoting the surface superhydrophobicity. In this experiment, near-ideal grooves are fabricated on the FeCoCrMnNi surface by the nanosecond pulse laser, and the burrs and resolidified layers produced during laser processing are avoided as far as possible.

The structural features of grooves depend mainly on the laser power and number of scans when the scanning speed is fixed. Therefore, by varying these two parameters during experiments, the grooves with large depth-to-width ratios could be constructed. Figures 2(c)–2(f) present the structural features of grooves at different laser powers and number of scans. As shown in Fig. 2(c), the width of the grooves gradually increases with increasing laser power. This is a very common phenomenon, where the material on both sides of the groove is gradually ablated due to the increased laser energy. However, the depth of groove first climbs up and then declines as the laser power increases. When the laser power increases from 4.2 to 9.7 W, the depth of the groove increases from 1.5 to 9  $\mu\text{m}$ . While further increasing the laser power to 13.4 W, the depth of groove decreases to 5  $\mu\text{m}$ . This decrease in depth may be due to the flow of the surrounding melting material into the groove. Figure 2(d) shows the curves for variation of the depth-to-width ratio with the laser power, and it can be concluded that a groove with a stable and large depth-to-width ratio can be achieved when the laser power reaches 9.7 W. On this basis, single-line scanning experiments with different number of scans were further performed. As shown in Fig. 2(e), as the number of scans increases, the depth and width of groove increase accordingly. When the number of scans reaches 3, the grooves have a stable and large depth-to-width ratio of 0.175. This ratio ultimately is related to the type of laser and material. Under the selected laser parameters ( $P=9.7$  W,  $v=10$  mm/s,  $N=3$ ), the arrays with large depth-to-width ratios and different hatching intervals were constructed on the FeCoCrMnNi surface for achieving superhydrophobicity.

Figures 3(a)–3(d) present the SEM morphologies of arrays at different hatching intervals. As illustrated in Fig. 3, all arrays consist of intersecting grooves. When the laser power is 9.7 W and the scan number is 3, the width of the groove is measured to be about 85  $\mu\text{m}$ . At a hatching interval of 50  $\mu\text{m}$ , the entire surface of the material is irradiated by laser. However, due to the Gaussian distribution of the laser energy, some materials are completely ablated, and the molten materials flow to both sides due to the recoil pressure. After several scans, the molten materials are resolidified to form an array structure, being similar to a cylinder. When the hatching interval exceeds 85  $\mu\text{m}$ , some unirradiated regions remain on the original surface. As a result, the redesigned cube arrays are formed rather than cylinders. However, some metal particles still appear on the array surface. These particles are formed through melt sputtering caused by the recoil pressure as well as the

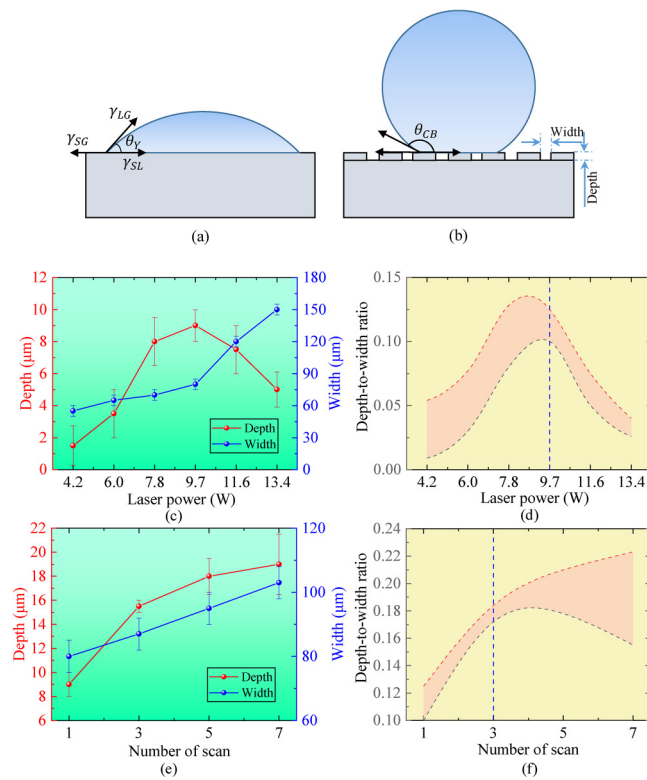
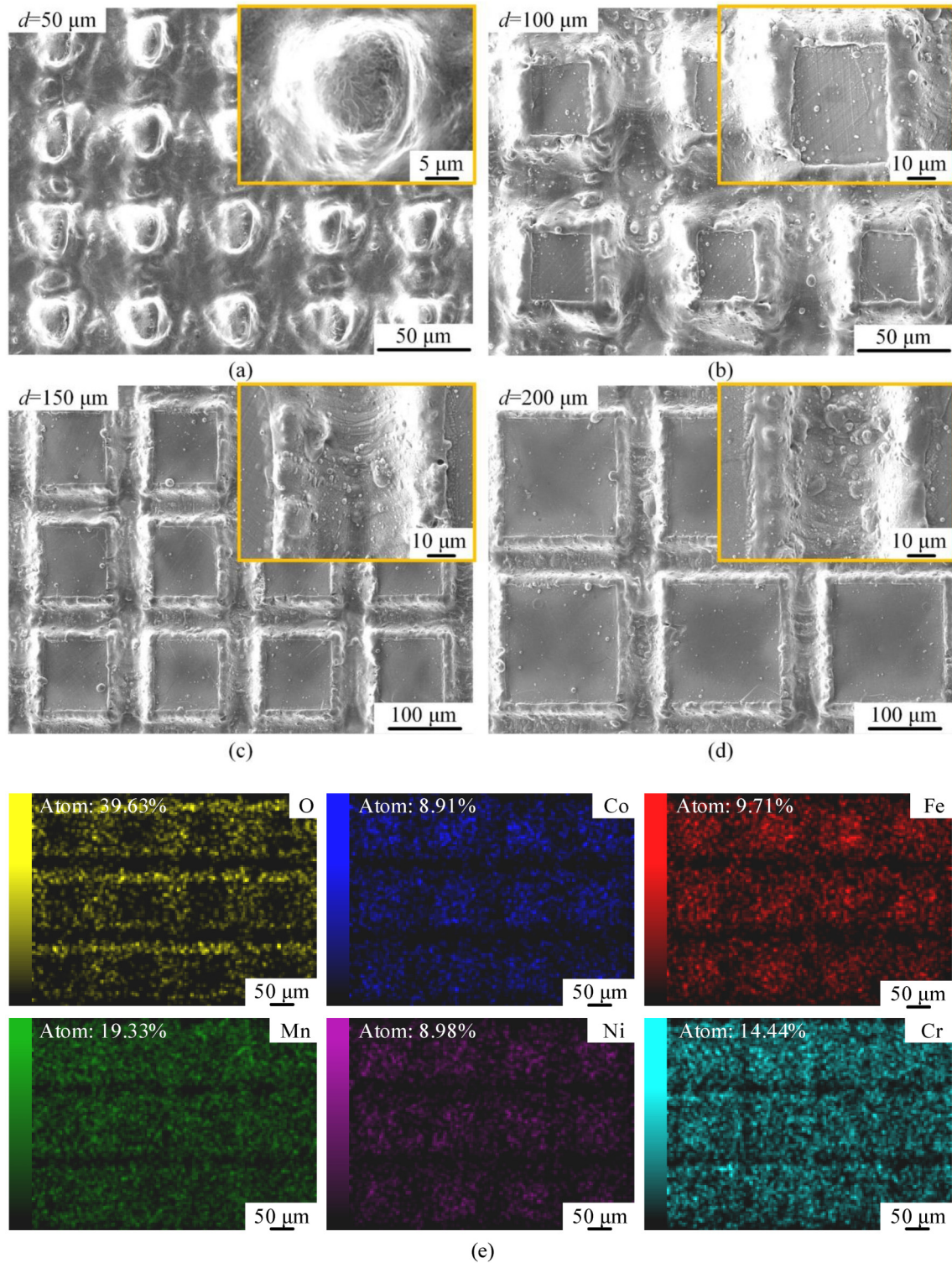


FIG. 2. (a) Young’s angle  $\theta_Y$  on a flat surface, (b) Cassie–Baxter’s angle  $\theta_{CB}$  on a textured surface. (c) Depth and width as well as (d) depth-to-width ratio of grooves changing with the laser power ( $v=10$  mm/s). (e) Depth and width as well as (f) depth-to-width ratio of grooves changing with the number of scans ( $v=10$  mm/s,  $P=9.7$  W).

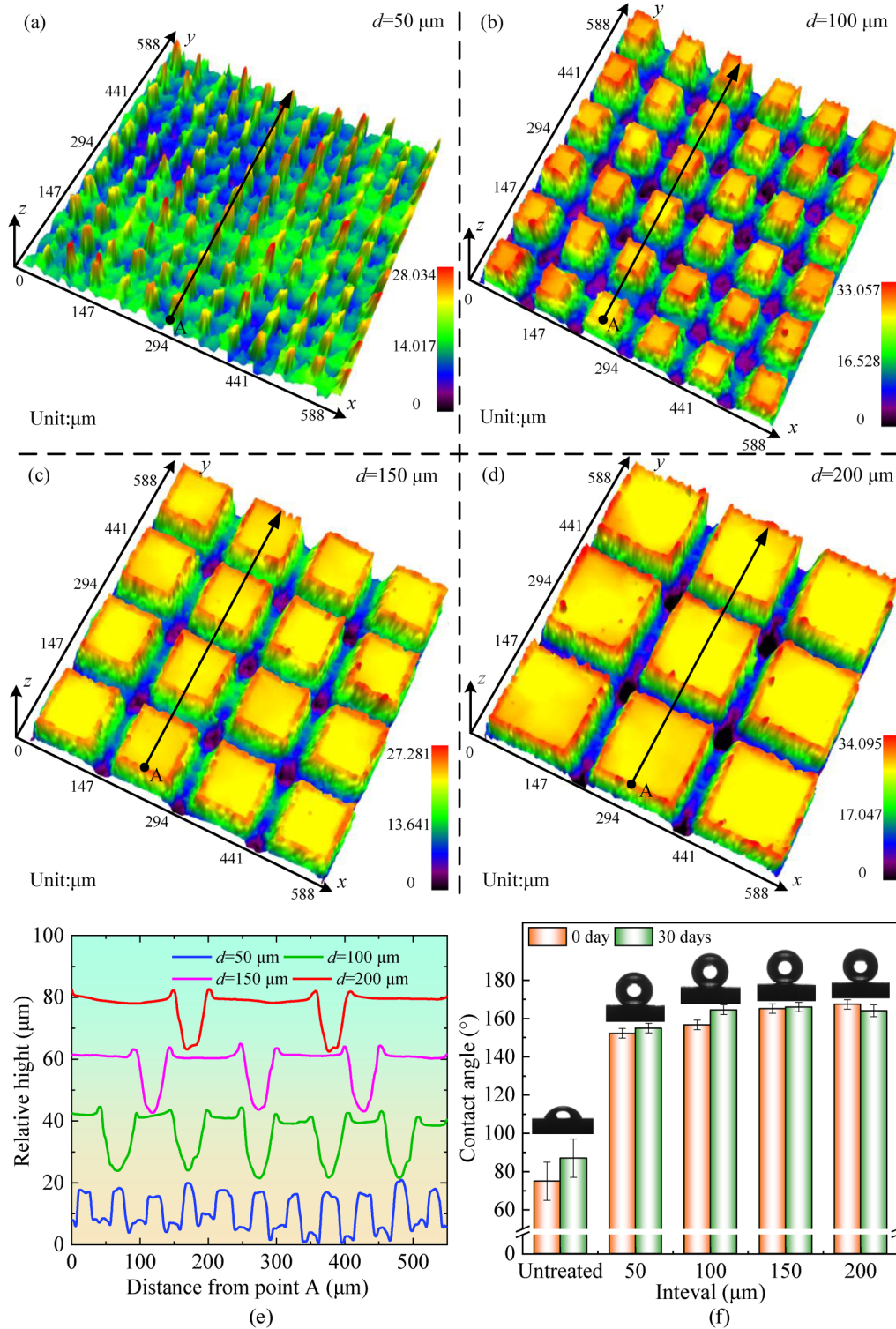
06 March 2024 02:15:03





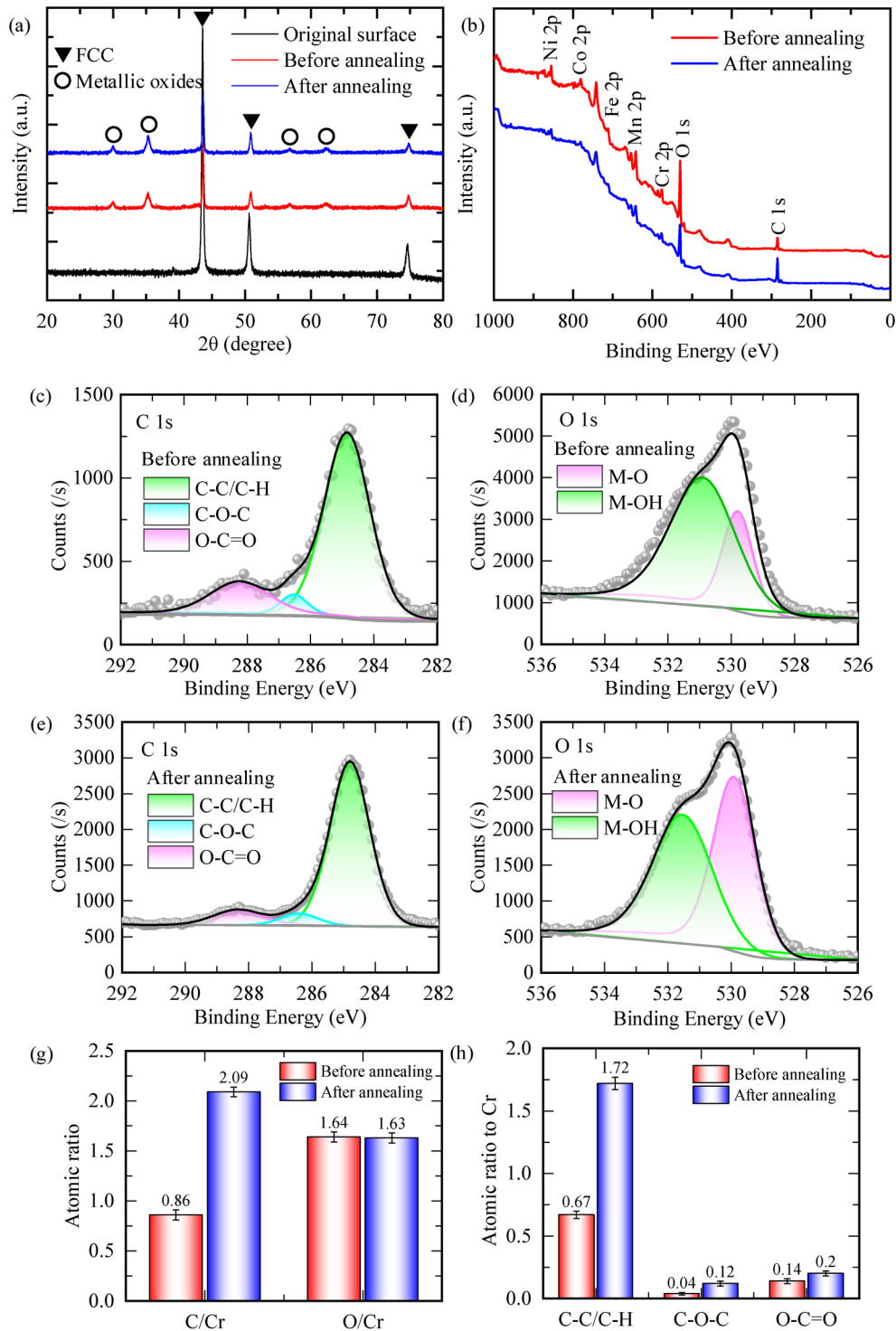
06 March 2024 02:15:03

**FIG. 3.** SEM morphologies of arrays with different hatching intervals  $d$ : (a) 50, (b) 100, (c) 150, and (d)  $200 \mu\text{m}$ . The enlarged images are located in the upper right of each image. (e) The EDS mapping of Fig. 3(c).



06 March 2024 02:15:03

**FIG. 4.** 3D topographies of the arrays with different hatching intervals  $d$ : (a) 50, (b) 100, (c) 150, and (d) 200  $\mu\text{m}$ . (e) Cross-sectional profiles corresponding to the solid lines in (a)–(d). (f) The contact angle of the original surface and laser textured surfaces after exposing to air for 0 day and 30 days. All surfaces were annealed.



06 March 2024 02:15:03

**FIG. 5.** (a) XRD patterns of the original surface and laser textured surfaces ( $d = 150 \mu\text{m}$ ) before and after annealing. (b) XPS spectrum and (c)–(f) high resolution C 1s and O 1s spectrums of laser textured surfaces ( $d = 150 \mu\text{m}$ ) before and after annealing. Atomic ratios to Cr of (g) C and O as well as (h) C–C/C–H, C–O–C, and O–C=O species on laser textured surfaces ( $d = 150 \mu\text{m}$ ) before and after annealing.



subsequent solidification of metal vapor as the plasma plume expands outwards.<sup>32,33</sup> Figure 3(e) shows the EDS mapping of Fig. 3(c). The O element is mainly enriched on both sides of grooves with a relatively large atomic ratio of 39.63%. The distribution of metal elements corresponds to that of the O element. The five elements exhibit different atomic ratios on the laser-ablated surface and their order corresponds to the metal activity series ( $Mn > Cr > Fe > Co \approx Ni$ ).

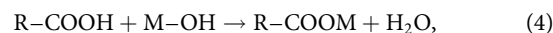
Figures 4(a)–4(d) show the 3D topographies of arrays with different hatching intervals, which display a remarkably uniform overall topography. The cross-sectional profiles of arrays with different hatching intervals are illustrated in Fig. 4(e). The depth and width of the grooves remain relatively consistent, which proves the good precision of the laser process. As shown in Video S1,<sup>38</sup> the fresh laser textured surface exhibits superhydrophilicity with a contact angle being approximately  $0^\circ$  due to the generation of metal oxides with high surface free energy.<sup>21</sup> Therefore, all surfaces are annealed to achieve lower surface free energy in this experiment, and the corresponding contact angles are shown in Fig. 4(f). After annealing, the contact angle of the untreated original surface is  $75^\circ$ , indicating its inherent hydrophilicity. However, all laser textured surfaces with different hatching intervals demonstrate excellent superhydrophobicity, with contact angles greater than  $150^\circ$ , as depicted in Video S2.<sup>38</sup> In particular, at a hatching interval of  $150\ \mu\text{m}$ , the contact angle reaches  $165^\circ$ . The above experimental results indicate that superhydrophobicity could be achieved on the FeCoCrMnNi surface by laser texturing and subsequent annealing at a low temperature. After exposing to the air for 30 days, the contact angles of textured surfaces remain almost constant, suggesting that such superhydrophobic surfaces can be stored in ambient air for a long time.

To investigate the underlying mechanisms of wettability transition on FeCoCrMnNi surface, the surface chemical composition of the laser textured surfaces before and after annealing is further characterized. Figure 5(a) shows the XRD patterns of the original surface and laser textured surfaces before and after annealing. In Fig. 5(a), the original surface consists of a single fcc phase, which is consistent with previous studies.<sup>34</sup> During the laser processing, some metallic oxides are produced on the laser textured surfaces. The metallic oxides may contain  $\text{Fe}_3\text{O}_4$ ,  $\text{NiCr}_2\text{O}_4$ ,  $\text{MnCr}_2\text{O}_4$ ,  $\text{CoCr}_2\text{O}_4$ , and  $\text{NiFe}_2\text{O}_4$  by comparative analysis of XPS and PDF cards. However, the peak intensity and position of metallic oxides before and after annealing remain almost identical, indicating that the metallic oxides are not the reason leading to the wettability transition of laser textured surface.

Figures 5(b)–5(f) show the XPS spectrum of laser textured surfaces before and after annealing. Metallic elements (Ni, Co, Fe, Mn, Cr) as well as C and O elements are detected in this spectrum. The high resolution C 1s spectrum is composed of three peaks of  $\sim 284.8$ ,  $286.3$ , and  $288.5$  eV, which represent the C–C/C–H, C–O–C, and O–C=O, respectively. The high resolution O 1s spectrum consists of two peaks of  $\sim 529.5$  and  $531$  eV, which represent lattice oxygen (M–O) and the oxygen associated with the hydroxyls (M–OH), respectively.<sup>22,23</sup> It can be seen from Fig. 5(g) that after annealing, the atomic ratio (C/Cr) on the laser textured surface increases significantly while the atomic ratio (O/Cr) remains unchanged. This suggests that the superhydrophobicity of laser

textured surface after annealing is related to the increase of C content. Therefore, the changes in the atomic ratios of three relevant functional groups to Cr are illustrated in Fig. 5(h). The functional group C–C/C–H is nonpolar, which is associated with hydrophobicity. In contrast, the functional group C–O–C/O–C=O is polar, which is associated with hydrophilicity.<sup>21,25</sup> After annealing, the atomic ratio of functional group C–C/C–H significantly increases from 0.67 to 1.72, while the atomic ratio of functional group O–C=O increases slightly, which contributes to the wettability transition from superhydrophilicity to superhydrophobicity.

After laser texturing, the resulting surfaces are unbalanced, with high surface polarity, thus exhibiting surface superhydrophilicity.<sup>21</sup> However, after short annealing at low temperature, the non-polar functional group C–C/C–H increases dramatically on the laser textured surface. Consequently, the total surface free energy decreases, resulting in a transition from superhydrophilicity to superhydrophobicity.<sup>35</sup> The changes in the content of functional groups are generally attributed to the absorption of airborne organic compounds during the annealing process through the chemisorption between the hydroxyl on the laser textured surface and the carboxyl of airborne organic compounds.<sup>25</sup> The schematic diagram of the chemisorption is illustrated in Fig. 6, and it can be expressed by the following equation:<sup>22</sup>



where R, M, and R–COOM represent alkyl, metal atoms, and carboxylates, respectively.

Figure 7(a) presents the drop impact dynamics on the arrays with  $d = 150\ \mu\text{m}$ . Typical droplet bouncing behavior could be observed on the constructed superhydrophobic surface. As shown in Fig. 7(a), the impacting droplet first contacts the textured surface, and then undergoes a series of processes (pancake, shrinkage, splitting, and pinning) before finally bouncing up from the surface.<sup>36</sup> During droplet bouncing, the pinning phenomenon occurs, resulting in a significant reduction in the droplet's kinetic energy. Furthermore, the droplet splitting is caused by the difference in shrinkage speed between the top and bottom of the droplet due to the pinning phenomenon.<sup>37</sup> Dropping from a height of

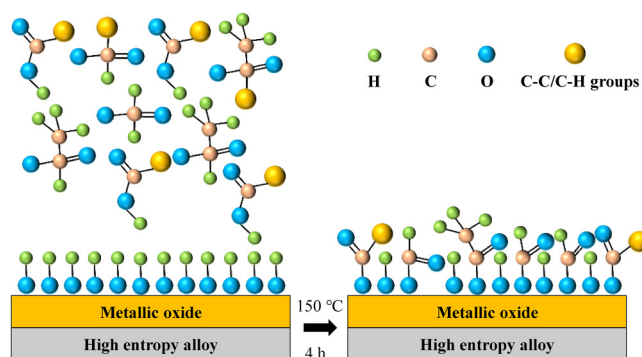
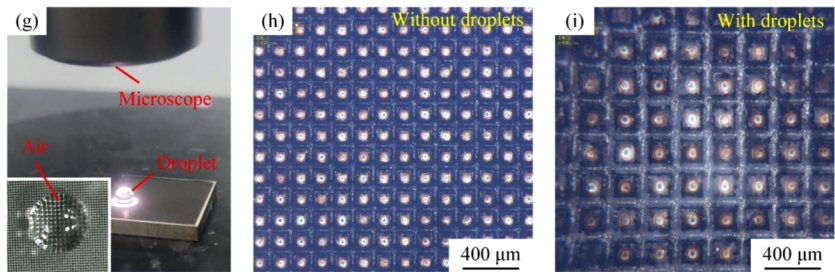
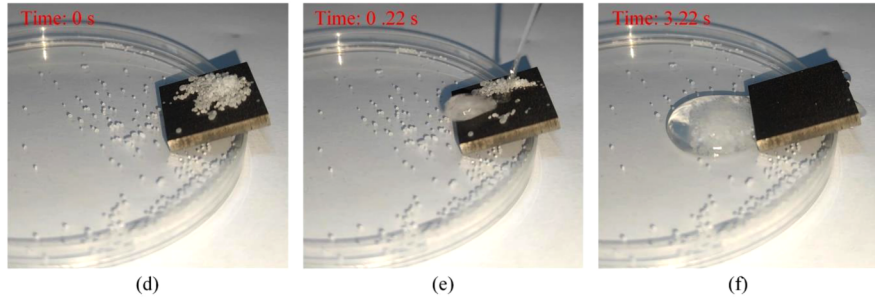
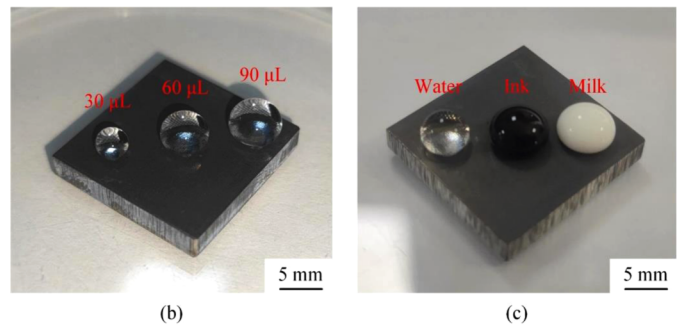
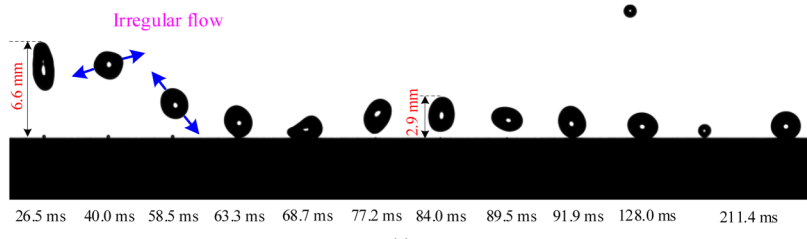
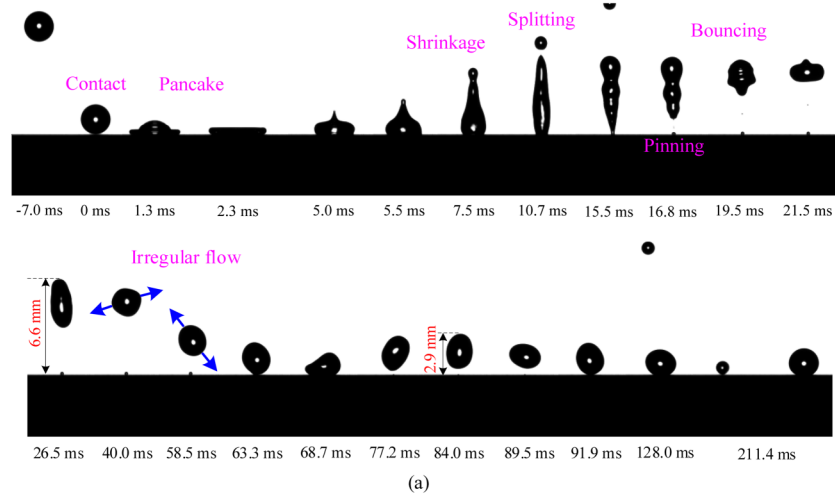


FIG. 6. The schematic diagram of the chemisorption between the hydroxyl on the laser textured surface and carboxyl of airborne organic compounds.

06 March 2024, 02:15:03



**FIG. 7.** (a) Drop impact dynamics on the laser textured surface ( $d = 150 \mu\text{m}$ ). The droplet diameter and impact height are 2.1 and 50 mm, respectively. Optical images of some droplets with (b) different volumes (30, 60, and  $90 \mu\text{L}$ ) and (c) liquid mediums (water, ink, and milk). (d)–(f) Self-cleaning procedure during which water droplets are carried away the white powder on the laser textured surface ( $d = 150 \mu\text{m}$ ). (g) Optical image of solid-liquid contact state on the laser textured surface ( $d = 150 \mu\text{m}$ ). The optical images of arrays (h) without droplets and (i) with droplets.

06 March 2024 02:15:03



50 mm, the droplet undergoes only two bouncing processes. The height of the first bounce is drastically reduced to 13% (6.6 mm), which facilitates the capture and collection of droplets in practical applications. **Figures 7(b) and 7(c)** show the optical images of some droplets with different water volumes (30, 60, and 90  $\mu\text{l}$ ) and liquid mediums (water, ink, and milk) on the laser textured surface. When the volume of droplet increases, the droplet gradually appears as a dome due to the gravity but still retains excellent superhydrophobicity. For different types of liquid mediums, the textured surfaces exhibit good water repellency. The created superhydrophobic surface of FeCoCrMnNi could be applied for self-cleaning applications. As shown in **Figs. 7(d)–7(f)**, sliding water droplets are capable of cleaning the sample surface that is covered in white powder (salt). From the inset of **Fig. 7(g)**, the air is trapped between the droplets and structures, preventing the droplet from infiltrating the textured surface, which displays a typical Cassie–Baxter state. **Figures 7(h) and 7(i)** show the optical images of arrays covering with and without droplets, taken at the same magnification. The droplets on the superhydrophobic surface act as a convex lens to magnify the image.

#### IV. CONCLUSIONS

Superhydrophobicity was successfully achieved on the FeCoCrMnNi surface via synergistic laser texturing and low temperature annealing. By optimizing the laser parameters (laser power and number of scans), the arrays consisting of near-ideal grooves with large depth-to-width ratios were constructed, followed by annealing at low temperature to achieve the transition from superhydrophilicity to superhydrophobicity. XRD and XPS analyses revealed that this wettability transition was attributed to the absorption of airborne organic compounds, independent of the metallic oxide formation. The textured surfaces exhibited excellent superhydrophobicity at different hatching intervals and a maximum contact angle of  $165^\circ$  was obtained. The constructed superhydrophobic surface demonstrated good liquid capture, self-cleaning capabilities, and the ability to magnify optical images. The stable superhydrophobicity in the Cassie–Baxter state was attributed to the synergistic effect of the arrays with large depth-to-width ratios as well as the adsorption of airborne organic compounds. Overall, this study provides a cost-effective, environmentally friendly, and versatile strategy for achieving superhydrophobicity of the FeCoCrMnNi surface.

#### ACKNOWLEDGMENTS

This work was supported by the Natural Science Foundation of Jilin Province (No. 20220101198JC) and the Fundamental Research Funds for the Central Universities (2020–2023).

#### AUTHOR DECLARATIONS

##### Conflicts of Interest

The authors have no conflicts to disclose.

#### Author Contributions

**Chao Wang:** Data curation (lead); Formal analysis (lead); Investigation (lead); Validation (lead); Visualization (lead); Writing – original draft (lead). **Hu Huang:** Conceptualization (lead); Funding acquisition (lead); Investigation (equal); Methodology (lead); Project administration (lead); Resources (lead); Supervision (lead); Writing – review & editing (lead). **Mingming Cui:** Data curation (equal); Investigation (equal); Validation (equal). **Zhiyu Zhang:** Data curation (equal); Investigation (equal). **Lin Zhang:** Data curation (equal); Investigation (equal). **Jiawang Yan:** Methodology (equal); Supervision (equal).

#### REFERENCES

- 1 J. W. Yeh, S. K. Chen, S. J. Lin, J. Y. Gan, T. S. Chin, T. T. Shun, C. H. Tsau, and S. Y. Chang, “Nanostructured high-entropy alloys with multiple principal elements: Novel alloy design concepts and outcomes,” *Adv. Eng. Mater.* **6**, 299 (2004).
- 2 B. Cantor, I. T. H. Chang, P. Knight, and A. J. B. Vincent, “Microstructural development in equiatomic multicomponent alloys,” *Mater. Sci. Eng., A* **375–377**, 213 (2004).
- 3 B. Gludovatz, A. Hohenwarter, D. Catoor, E. H. Chang, E. P. George, and R. O. Ritchie, “A fracture-resistant high-entropy alloy for cryogenic applications,” *Science* **345**, 1153 (2014).
- 4 S. Son, P. Asghari-Rad, A. Zargar, W. Chen, and H. S. Kim, “Superlative room temperature and cryogenic tensile properties of nanostructured CoCrFeNi medium-entropy alloy fabricated by powder high-pressure torsion,” *Scr. Mater.* **213**, 114631 (2022).
- 5 K. Lu, A. Chauhan, D. Litvinov, A. S. Tirunilai, J. Freudenberger, A. Kauffmann, M. Heilmaier, and J. Aktaa, “Micro-mechanical deformation behavior of CoCrFeMnNi high-entropy alloy,” *J. Mater. Sci. Technol.* **100**, 237 (2022).
- 6 Y. Shi, B. Yang, and P. Liaw, “Corrosion-resistant high-entropy alloys: A review,” *Metals* **7**, 43 (2017).
- 7 J. Chen, X. Zhou, W. Wang, B. Liu, Y. Lv, W. Yang, D. Xu, and Y. Liu, “A review on fundamental of high entropy alloys with promising high-temperature properties,” *J. Alloys Compd.* **760**, 15 (2018).
- 8 K. Jin, C. Lu, L. M. Wang, J. Qu, W. J. Weber, Y. Zhang, and H. Bei, “Effects of compositional complexity on the ion-irradiation induced swelling and hardening in Ni-containing equiatomic alloys,” *Scr. Mater.* **119**, 65 (2016).
- 9 Z. U. Arif, M. Y. Khalid, E. ur Rehman, S. Ullah, M. Atif, and A. Tariq, “A review on laser cladding of high-entropy alloys, their recent trends and potential applications,” *J. Manuf. Process.* **68**, 225 (2021).
- 10 P. Wang, X. Yan, J. Zeng, C. Luo, and C. Wang, “Anti-reflective superhydrophobic coatings with excellent durable and self-cleaning properties for solar cells,” *Appl. Surf. Sci.* **602**, 154408 (2022).
- 11 Y. X. Shu, X. Y. Lu, Y. F. Liang, W. B. Su, W. Gao, J. J. Yao, Z. Niu, Y. Lin, and Y. L. Xie, “Nanosecond laser fabrication of superhydrophobic copper and anti-frost surface on copper,” *Surf. Coat. Technol.* **441**, 128514 (2022).
- 12 I. Vilaró, J. L. Yagüe, and S. Borrós, “Superhydrophobic copper surfaces with anticorrosion properties fabricated by solventless CVD methods,” *ACS Appl. Mater. Interfaces* **9**, 1057 (2017).
- 13 Y. Tang, X. L. Yang, Y. M. Li, Y. Lu, and D. Zhu, “Robust micro-nanostructured superhydrophobic surfaces for long-term dropwise condensation,” *Nano Lett.* **21**, 9824 (2021).
- 14 H. Liu, Y. D. Wang, J. Y. Huang, Z. Chen, G. Q. Chen, and Y. K. Lai, “Bioinspired surfaces with superamphiphobic properties: Concepts, synthesis, and applications,” *Adv. Funct. Mater.* **28**, 1707415 (2018).
- 15 J. Peng, X. Zhao, W. Wang, and X. Gong, “Durable self-cleaning surfaces with superhydrophobic and highly oleophobic properties,” *Langmuir* **25**, 8404–8412 (2019).

- <sup>16</sup>D. Wang, Q. Sun, M. J. Hokkanen, C. Zhang, F. Y. Lin, Q. Liu, S. P. Zhu, T. Zhou, Q. Chang, B. He, Q. Zhou, L. Chen, Z. Wang, R. H. A. Ras, and X. Deng, "Design of robust superhydrophobic surfaces," *Nature* **582**, 55 (2020).
- <sup>17</sup>W. Tong and D. S. Xiong, "Direct laser texturing technique for metal surfaces to achieve superhydrophobicity," *Mater. Today Phys.* **23**, 100651 (2022).
- <sup>18</sup>N. G. Tran and D. M. Chun, "Ultrafast and eco-friendly fabrication process for robust, repairable superhydrophobic metallic surfaces with tunable water adhesion," *ACS Appl. Mater. Interfaces* **14**, 28348 (2022).
- <sup>19</sup>G. Zhao, G. Zou, W. Wang, R. Geng, X. Yan, Z. He, L. Liu, X. Zhou, J. Lv, and J. Wang, "Competing effects between condensation and self-removal of water droplets determine antifrosting performance of superhydrophobic surfaces," *ACS Appl. Mater. Interfaces* **12**, 7805 (2020).
- <sup>20</sup>H. H. Nguyen, A. K. Tieu, S. Wan, H. Zhu, S. T. Pham, and B. Johnston, "Surface characteristics and wettability of superhydrophobic silanized inorganic glass coating surfaces textured with a picosecond laser," *Appl. Surf. Sci.* **537**, 147808 (2021).
- <sup>21</sup>J. Long, M. Zhong, H. Zhang, and P. Fan, "Superhydrophilicity to superhydrophobicity transition of picosecond laser microstructured aluminum in ambient air," *J. Colloid Interface Sci.* **441**, 1 (2015).
- <sup>22</sup>Z. Yang, X. Liu, and Y. Tian, "Insights into the wettability transition of nanosecond laser ablated surface under ambient air exposure," *J. Colloid Interface Sci.* **533**, 268 (2019).
- <sup>23</sup>C.-V. Ngo and D.-M. Chun, "Fast wettability transition from hydrophilic to superhydrophobic laser-textured stainless steel surfaces under low-temperature annealing," *Appl. Surf. Sci.* **409**, 232 (2017).
- <sup>24</sup>C. Ma, M. Kang, N. J. Ndiithi, and X. Wang, "Wettability transition of the picosecond laser-ablated 304 stainless-steel surface via low-vacuum heat treatment," *Langmuir* **37**, 14314 (2021).
- <sup>25</sup>X. Li, Y. Jiang, Z. Jiang, Y. Li, C. Wen, and J. Lian, "Reversible wettability transition between superhydrophilicity and superhydrophobicity through alternate heating-reheating cycle on laser-ablated brass surface," *Appl. Surf. Sci.* **492**, 349 (2019).
- <sup>26</sup>H. Exir and A. Weck, "Mechanism of superhydrophilic to superhydrophobic transition of femtosecond laser-induced periodic surface structures on titanium," *Surf. Coat. Technol.* **378**, 124931 (2019).
- <sup>27</sup>A. M. Kietzig, S. G. Hatzikiriakos, and P. Englezos, "Patterned superhydrophobic metallic surfaces," *Langmuir* **25**, 4821 (2009).
- <sup>28</sup>F.-M. Chang, S.-L. Cheng, S.-J. Hong, Y.-J. Sheng, and H.-K. Tsao, "Superhydrophilicity to superhydrophobicity transition of CuO nanowire films," *Appl. Phys. Lett.* **96**, 114101 (2010).
- <sup>29</sup>J. Li, Y. Zhou, W. Wang, C. Xu, and L. Ren, "Superhydrophobic copper surface textured by laser for delayed icing phenomenon," *Langmuir* **36**, 1075 (2020).
- <sup>30</sup>K. Mądry and W. Nowicki, "Wetting between Cassie-Baxter and Wenzel regimes: A cellular model approach," *Eur. Phys. J. E* **44**, 138 (2021).
- <sup>31</sup>S. Haj Ibrahim, T. Wejrzanowski, B. Przybyszewski, R. Kozera, X. García-Casas, and A. Barranco, "Role of surface topography in the superhydrophobic effect—Experimental and numerical studies," *Materials* **15**, 3112 (2022).
- <sup>32</sup>I. Bitharas, N. Parab, C. Zhao, T. Sun, A. D. Rollett, and A. J. Moore, "The interplay between vapour, liquid, and solid phases in laser powder bed fusion," *Nat. Commun.* **13**, 2959 (2022).
- <sup>33</sup>S. Ly, A. M. Rubenchik, S. A. Khairallah, G. Guss, and M. J. Matthews, "Metal vapor micro-jet controls material redistribution in laser powder bed fusion additive manufacturing," *Sci. Rep.* **7**, 4085 (2017).
- <sup>34</sup>S. H. Shim, J. Moon, H. Pouraliakbar, B. J. Lee, S. I. Hong, and H. S. Kim, "Toward excellent tensile properties of nitrogen-doped CoCrFeMnNi high-entropy alloy at room and cryogenic temperatures," *J. Alloys Compd.* **897**, 163217 (2022).
- <sup>35</sup>M. Cui, H. Huang, C. Wang, L. Zhang, and J. Yan, "Achieving superhydrophobicity of Zr-based metallic glass surfaces with tunable adhesion by nanosecond laser ablation and annealing," *ACS Appl. Mater. Interfaces* **14**, 39567 (2022).
- <sup>36</sup>Y. Liu, L. Moevius, X. Xu, T. Qian, J. M. Yeomans, and Z. Wang, "Pancake bouncing on superhydrophobic surfaces," *Nat. Phys.* **10**, 515 (2014).
- <sup>37</sup>C. Hao, Y. Liu, X. Chen, J. Li, M. Zhang, Y. Zhao, and Z. Wang, "Bioinspired interfacial materials with enhanced drop mobility: From fundamentals to multi-functional applications," *Small* **12**, 1825 (2016).
- <sup>38</sup>See supplementary material online for the dynamic contact process between the droplet and the fresh laser textured surface, exhibiting superhydrophilicity with a contact angle being approximately  $0^\circ$  (video S1) and the dynamic contact process between the droplet and the annealed laser textured surface, exhibiting superhydrophobicity with a contact angle being greater than  $150^\circ$  (video S2).